

Coexisted Three-component Bosons and Two-component Weyl Bosons in TiS, ZrSe and HfTe

Jiangxu Li,¹ Qing Xie,^{1,2} Sami Ullah,^{1,2} Ronghan Li,¹ Hui Ma,¹ Dianzhong Li,¹ Yiyi Li,¹ and Xing-Qiu Chen^{1,*}

¹*Shenyang National Laboratory for Materials Science, Institute of Metal Research,
Chinese Academy of Science, School of Materials Science and Engineering,
University of Science and Technology of China, 110016, Shenyang, China*

²*University of Chinese Academy of Sciences, Beijing, 100049, China*

(Dated: October 27, 2021)

In analogy to various fermions of electrons in topological semimetals, topological mechanical states with two type of bosons, Dirac and Weyl bosons, were reported in some macroscopic systems of kHz frequency and those with a type of doubly-Weyl phonons in atomic vibrational framework of THz frequency of solid crystals were recently predicted. However, to date no three-component bosons of phonon has been reported. Here, through first-principles calculations, we have reported that the phonon spectra of the WC-type TiS, ZrSe, and HfTe commonly host the unique triply degenerate nodal points (TDNPs) and single two-component Weyl points (WPs) in THz frequency. Quasiparticle excitations near TDNPs of phonons are three-component bosons, beyond the conventional and known classifications of Dirac, Weyl and doubly-Weyl phonons. Moreover, we have found that both TiS and ZrSe have five pairs of type-I Weyl phonons and a pair of type-II Weyl phonons, whereas HfTe only has four pairs of type-I Weyl phonons. They carry non-zero topological charges. On the (10 $\bar{1}$ 0) crystal surfaces, we observe topological protected surface arc states connecting two WPs with opposite charges, which host modes that propagate nearly in one direction on the surface.

I. INTRODUCTIONS

Topological semimetals [1–5] are one of the fast growing families in the frontier of material sciences and condensed matter physics due to their unique density of states, transport properties and novel topological surface states as well as their potential for use in quantum computers, spintronics and novel physics. It has been well-known that topological semimetals highlight several main types of interesting fermions in crystal solids, such as three-dimensional (3D) Dirac cones [6–16], Weyl nodes [17–35], Dirac nodal lines [39–49], triply degenerate nodal points [54–63], and even beyond [54]. In addition, their realization in crystal solids is also important because they provide the ways to study elementary particles, which were long-sought and predicted ones, in high-energy physics. Importantly, in similarity to various fermions of electrons, the exciting progresses of the bosons (vibrational phonons) have been also predicted [64] or observed in the 3D momentum space of solid crystals with the topological vibrational states, such as Dirac, Weyl and line-node phonons in photonic crystals only with macroscopic systems of kHz frequency [64–79] and, even most recently, theoretically predicted doubly-Weyl phonons in transition-metal monosilicides with atomic vibrations at THz frequency [80]. However, to date no three-component bosons have been reported, although three-component fermions have been experimentally discovered in the most recent work of MoP [61].

The three-component bosons would possibly occur in atomic solid crystals because three-fold degeneracy can

be protected by lattice symmetries, such as symmorphic rotation combined with mirror symmetries and non-symmorphic symmetries, as what was already demonstrated to be triply degenerated points of electronic fermions in the solid crystals [54–61]. In addition to the importance of seeking the new type of three-component bosons, the topological phononic states will be extremely interesting because they could certainly enable materials to exhibit novel heat transfer, phonon scattering and electron-phonon interactions, as well as other properties related with vibrational modes, such as thermodynamics. In the first, in similarity to topological properties of electrons, the topological effects of phonons can induce the one-way edge phonon states (the topologically protected boundary states). These states will conduct phonon with little or no scattering [74, 77], highlighting possible applications for designing phononic circuits [82]. Utilizing the one-way edge phonon states an ideal phonon diode [82] with fully 100% efficiency becomes potential in a multi-terminal transport system. In the second, in different from that of electrons, as one of bosons, phonons, are not limited by the Pauli exclusion principle. This fact demonstrates that the whole frequency zone of phonon spectrum can be physically probed. It was even theoretically demonstrated that the chiral phonons excited by polarized photons can be detected by a valley phonon Hall effect in monolayer hexagonal lattices [81]. Within this context, through first-principles calculations we report on the novel coexistence of the triply degenerate nodal points (TDNPs) and type-I and type-II Weyl nodes (WPs) of phonons in three compounds of TiS, ZrSe and HfTe. Interestingly, these three materials simultaneously still exhibit three-component fermions and two-component Weyl fermions from their electronic structures. The coexistence of three-component bosons,

* Corresponding author: xingqiu.chen@imr.ac.cn

two-component Weyl bosons, three-component fermions and two-component Weyl fermions provide attractive candidates to study the interplays between topological phonons and topological fermions in the same solid crystals.

II. METHODS

Within the framework of the density functional theory (DFT) [83, 84] and the density functional perturbation theory (DFPT) [85], we have performed the calculations on the structural optimization, the electronic band structures, the phonon calculations and surface electronic band structures. Both DFT and DFPT calculations have been performed by employing the Vienna *ab initio* Simulation Package (VASP) [86–88], with the projector augmented wave (PAW) pseudopotentials [91, 92] and the generalized gradient approximation (GGA) within the Perdew-Burke-Ernzerhof (PBE) exchange-correlation functional [90]. The adopted PAW-PBE pseudopotentials of all elements treat semi-core valence electrons as valence electrons. A very accurate optimization of structural parameters have been calculated by minimizing the interionic forces below 0.0001 eV/\AA . The cut-off energy for the expansion of the wave function into the plane waves was 500 eV. The Brillouin zone integrations were performed on the Monkhorst-Pack k-meshes ($21 \times 21 \times 23$) and were sampled with a resolution of $2\pi \times 0.014 \text{ \AA}^{-1}$. The band structures, either with or without the inclusion of spin-orbit coupling (SOC), have been performed by the Gaussian smearing method with a width of smearing at 0.01 eV. Furthermore, the tight-binding (TB) through Green's function methodology [93–95] were used to investigate the surface states. We have calculated the Hamiltonian of tight-binding (TB) approach through maximally-localized Wannier functions (MLWFs) [96, 97] by using the Wannier 90code [98]. To calculate phonon dispersions, force constants are generated based on finite displacement method within the $4 \times 4 \times 4$ supercells using the VASP code and their dispersions have been further derived by Phonopy code [99]. We have also computed the phonon dispersions by including the SOC effect, which has been turned out to be no any influence in them. Furthermore, the force constants are used as the tight-binding parameters to build the dynamic matrices. We determine the topological charges of the WPs by using the Wilson-loop method [108, 109]. The surface phonon DOSs are obtained by using the iteration Green's function method [93].

III. RESULTS AND DISCUSSIONS

A. Crystal structure and structural stabilities of the *MX* compounds

Recently, the type of WC-type materials (Fig. 1(a)), including ZrTe, TaN, MoP and WC, has been theoretically reported to host the coexistence of the TDNPs and WPs in their electronic structures. This type of coexisted fermions of electronic TDNPs and WPs have been recently confirmed in MoP [61]. We further extended this family by proposing eight compounds (TiS, TiSe, TiTe, ZrS, ZrSe, HfS, HfSe and HfTe), which are isoelectronic and isostructural to ZrTe. Among these compounds, five compounds of TiS, ZrS, ZrSe_{0.90}, and Hf_{0.92}Se as well as ZrTe were experimentally reported to have the same WC-type structure [100–107]. No any experimental data is available for the remaining four compounds of TiSe, TiTe, HfS, and HfTe. Here, in order to systematically investigate their electronic structures and phonon spectra and to compare their differences, we have considered that all these nine compounds crystallize in the same WC-type structure. For five experimentally known compounds TiS, ZrS, ZrSe, ZrTe and HfSe, our DFT calculations yield the good agreement of their equilibrium lattice parameters with the experimental data (see supplementary Table S1). Their enthalpies of formation are derived in supplementary Table S1, indicating their stabilities in the thermodynamics and their phonon dispersions have no any imaginary frequencies, revealing the stabilities in the atomic mechanical vibrations.

B. Three-component fermions and two-component Weyl fermions in the electronic structures

We have elucidated the electronic band structures of these nine compounds. Interestingly, they are in similarity to the case of ZrTe in Ref. 57. As an example, the electronic band structure of ZrSe is given in the supplementary Fig. S1, indicating the coexisted fermions, TDNPs and WPs, whose coordinators are further compiled in Fig. 1c. Of course, the similar electronic behaviors can be observed for other compounds. But, TiS is unique. Because of its rather weak spin-orbit coupling (SOC) effect, TiS exhibits the coexistence of the six DNLs and the two six-fold degenerate nodal points of its electronic structure in the BZ. This situation is exactly what happens for other eight compounds when the SOC effect is ignored. Basically, the appearance of these two types of fermions, TDNPs and WPs, in this family share the same physics, as previously discussed for ZrTe [57]. The details of their electronic structures and their topologically protected non-trivial surface states refer to the supplementary Figs. S1, S2, S3, and S4 as well as the corresponding supplementary texts.

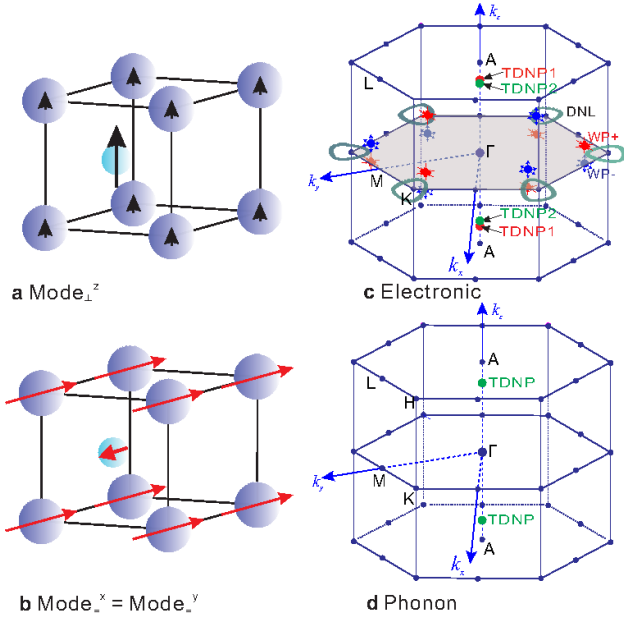


Figure 1. WC-type crystal structure and its Brillouin zone of MX ($M = \text{Ti, Zr, Hf}$; $X = \text{S, Se, Te}$). These materials crystallize in the simple hexagonal crystal structure with the space group of $P\bar{6}m2$ (No. 187). M occupies the $1a$ Wyckoff site (0, 0, 0) and X locates at the $1d$ ($1/3, 2/3, 1/2$) site. Panel (a) shows the phonon vertical vibrational mode (Mode_{\perp}^z) along the k_z direction at the boundary – the high-symmetry A (0, 0, $\pi/2$) point – of the Brillouin zone (BZ). Panel (b) denotes the phonon planar vibrational mode (Mode_{\perp}^x) along the k_x direction, which is two-fold degenerate ($\text{Mode}_{\perp}^x = \text{Mode}_{\perp}^y$) because of its C_{3v} rotational symmetry. Panel (c) The BZ in which the closed loops around each K point denotes the Dirac nodal lines (DNLs) of electrons around the Fermi level when SOC is ignored. With the SOC inclusion each DNL is broken into two Weyl points with the opposite chirality, marked as blue (WP-) and red (WP+) balls and they coexist with the triply degenerate nodal point (TDNP) of electronic structure (namely, three-component fermion). Panel (d) shows the triply degenerate nodal point (TDNP) of phonon dispersions (three-component boson) along the Γ -A direction in the BZ.

C. Triply degenerate nodal points (TDNPs) of the phonons in TiS, ZrSe and HfTe

We have found that the presence of the triply degenerate nodal points (TDNPs) of the phonons in three compounds of TiS, ZrSe and HfTe after a systematical analysis of their phonon dispersions (supplementary Fig. S5). Because each primitive cell contains two atoms (Fig. 1(a)), their phonon dispersions have six branches consisting of three acoustic and three optical ones, respectively. As compared with the computed phonon dispersions in Fig. 2(a, b, and c) and their phonon densities of states in Fig. 2(d, e, and f) of the isoelectronic ZrS, ZrSe and ZrTe compounds, a well-separated acoustic-optical gap can be observed in both ZrS and ZrTe with the smallest direct gap at the A point (0, 0, $\pi/2$) on the boundary of the

BZ. The specified analysis uncovered that for both ZrS and ZrTe compounds the top phonon band of the gap at the A point is comprised with the doubly degenerate vibrational mode of phonons in which both Zr and S (or Te) atoms, oppositely and collinearly, displace along either x or y direction ($\text{Mode}_{\perp}^{x,y}$ as marked in Fig. 1(b)). The vibrational amplitude of the $\text{Mode}_{\perp}^{x,y}$ are contributed nearly 100% by the Zr atom, rather than by S (or Te) atoms. The bottom phononic band of the gap at the A point is a singlet state originated from the vibrational mode at which both Zr and S (or Te) atoms collinearly move in the same k_z direction (Mode_{\perp}^z as marked in Fig. 1(a)). But its amplitude of this Mode_{\perp}^z are almost fully dominated by the displacement of S (or Te) atoms.

In contrast to both ZrS and ZrTe in Fig. 2, the case of ZrSe shows no acoustic-optical gap (Fig. 2(b)), as illustrated by its phonon density of states in 2(e)). It has been noted that the planar $\text{Mode}_{\perp}^{x,y}$ at the A point becomes now lower in frequency than the Mode_{\perp}^z . Accordingly, this fact corresponds to the occurrence of phonon band inversion at the A point. It means the unusual fact that around A point the optical phonon bands invert below the acoustic band which normally should have a lower frequency. Physically, within the (quasi)harmonic approximation the vibrational frequency, ω , have to be proportional to $\sqrt{\beta/m}$ at the boundary of the BZ. Here, β is the second-order force constant – the second derivative of the energy following a given vibrational mode as a function of the displacement and m the atomic mass. Therefore, as seen in Fig. 2(b) for ZrSe the occurrence of the phonon band inversion at the boundary A point is certainly induced by both β and m which are determined by the planar $\text{Mode}_{\perp}^{x,y}$ and the Mode_{\perp}^z at the A point. Following this consideration, we have defined the dimensionless ratio τ as follows,

$$\tau = \frac{\sqrt{\beta_{\perp}/m_{\perp}}}{\sqrt{\beta_{\parallel}/m_{\parallel}}}, \quad (1)$$

where τ specifies the comparison between the frequencies of both $\text{Mode}_{\perp}^{x,y}$ and Mode_{\perp}^z . With $\tau > 1$ the material shows no band inversion, thereby indicating no TDNPs. When $\tau < 1$ implies the appearance of the phonon band inversion with the TDNPs in the acoustic and optical gap. With such a definition, we further plot the β with the sequence of ZrS, ZrSe and ZrTe in Fig. 3(a). It has been found that, only with the second-order force constants of β_{\perp} and β_{\parallel} (Fig. 3(a)) it is not enough to induce the phonon band inversion. This fact is in agreement with the Eq. (1) although the $\beta_{\perp}-\beta_{\parallel}$ difference is the smallest in ZrSe among them in Fig. 3(a). Furthermore, for all nine compounds in this family we compiled their τ values as a function of the ratio (δ) of the atomic masses related with $\text{Mode}_{\perp}^{x,y}$ over Mode_{\perp}^z (namely, $\delta = m(\text{Mode}_{\perp}^{x,y})/m(\text{Mode}_{\perp}^z)$) in Fig. 3(b). With increasing the ratio of the atomic masses, the τ value increases in a nearly linear manner. This implies that, if the atomic masses of constituents in a targeted material highly differ, the possibility to have TDNPs in the acoustic and optical

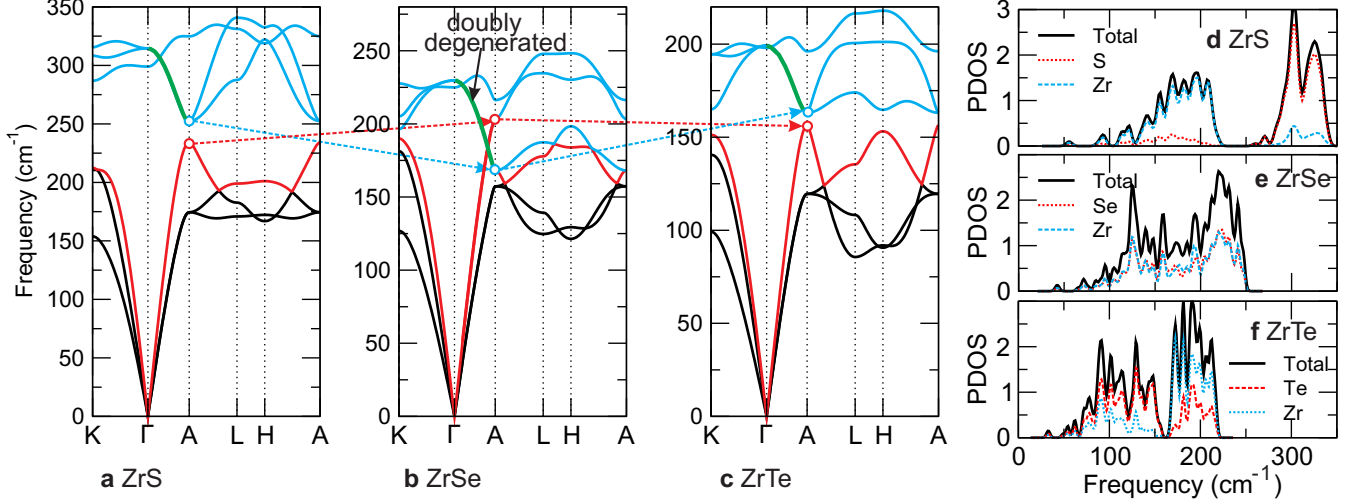


Figure 2. Phonon spectra of ZrS, ZrSe and ZrTe. Panels (a, b, and c): DFT-derived phonon dispersions of ZrS, ZrSe and ZrTe, respectively. Panels (d, e, and f): DFT-derived total and partial phonon densities of states (PDOS) of ZrS, ZrSe, and ZrTe, respectively.

gap of its phonon dispersion is extremely low. However, if they have the comparable atomic masses with the δ ratio close to 1 the possibility to have TDNPs is high in the acoustic and optical gap. Following this model, we have further uncovered that, because the τ value is smaller than 1, both TiS and HfTe have similar property as what ZrSe does (Fig. 3(b)). The findings for both TiS and HfTe are in accordance with the DFT-derived phonon dispersions in supplementary Fig. S5. However, there is no TDNP in the acoustic and optical gap of the other members. These facts imply that in these materials the difference between the atomic masses of constituents in compound plays a key role in inducing the phonon band inversion for the appearance of TDNPs in the acoustic and optical gap, as seen for three cases of TiS, ZrSe and HfTe whose δ value are all around 1.

Importantly, as accompanying with the occurrence of the phonon band inversion, the TDNPs, featured by a linear crossing of the frequencies between the acoustic and optical bands, unavoidably appear at $(0, 0, k_z = \pm 0.40769)$ along the Γ -A direction in the BZ (Fig. 2(b) and Fig. 3) for ZrSe. Their appearance of the TDNPs in the acoustic and optical gap is indeed protected by the C_{3z} rotation and mirror symmetries along the Γ -A direction because C_{3z} allows the coexistence of two-fold ($\text{Mode}_{\perp}^{x,y}$) and one-fold (Mode_{\perp}^z) representations, in similarity to their electronic band structures as discussed above. To elucidate the underlying mechanism of the phonon TDNPs in the acoustic and optical gap, it still needs to be emphasized that, on the one hand, the rotation and mirror symmetries substantially provide the prerequisite to produce these two competing modes (two-fold $\text{Mode}_{\perp}^{x,y}$ and one-fold Mode_{\perp}^z) and, on the other hand, the comparable atomic masses of constituent elements are another ingredient to trigger the phononic

band inversion. Of course, at this TDNP it still implies that the planar $\text{Mode}_{\perp}^{x,y}$ and the Mode_{\perp}^z at $(0, 0, k_z = \pm 0.40769)$ locate at the strictly same frequency of 183.9 cm^{-1} . The TDNPs locate at $(0, 0, k_z = \pm 0.40382)$ with the frequency of 293.4 cm^{-1} for TiS and at $(0, 0, k_z = \pm 0.43045)$ with the frequency of 133.3 cm^{-1} for HfTe. To elucidate the 3D TDNP shape of ZrSe, we also plot the zoom-in dispersions on both $k_z = 0$ and $k_y = 0$ planes of BZ in Fig. 3. From both Fig. 3(c) and 3(d) in the $k_z = 0$ the TDNP in the acoustic and optical gap can be clearly visualized to have an isotropic shape. However, in the $k_y = 0$ plane the phonon bands around the TDNPs are highly complex with the helicoid shape (Fig. 3(e) and 3(f)).

D. Two-component Weyl phonons in TiS, ZrSe and HfTe

Besides the existence of the TDNPs in TiS, ZrSe and HfTe, the calculations revealed the occurrence of the two-component Weyl nodes (WPs) in their phonon spectra. As evidenced in Fig. 4(a) for TiS, the phonon bands have five different band crossings (from C1 to C5) at the high-symmetry K point and a band crossing at the H point. In particular, because these crossings are not constrained by any mirror symmetry, they result in the appearance of six pairs of WPs (Table I). Among them, the band crossings from C1 to C5 confirm the five pairs of type-I WPs from WP1 to WP5 and the C6 crossing gives rise to the sixth pair of type-II WP6 one. The phonon dispersions of type-I and type-II WPs are shown in Fig. 4h and Fig. 4i, respectively. To identify their topological non-trivial properties, we have calculated the topological charge of each Weyl node, which is defined by

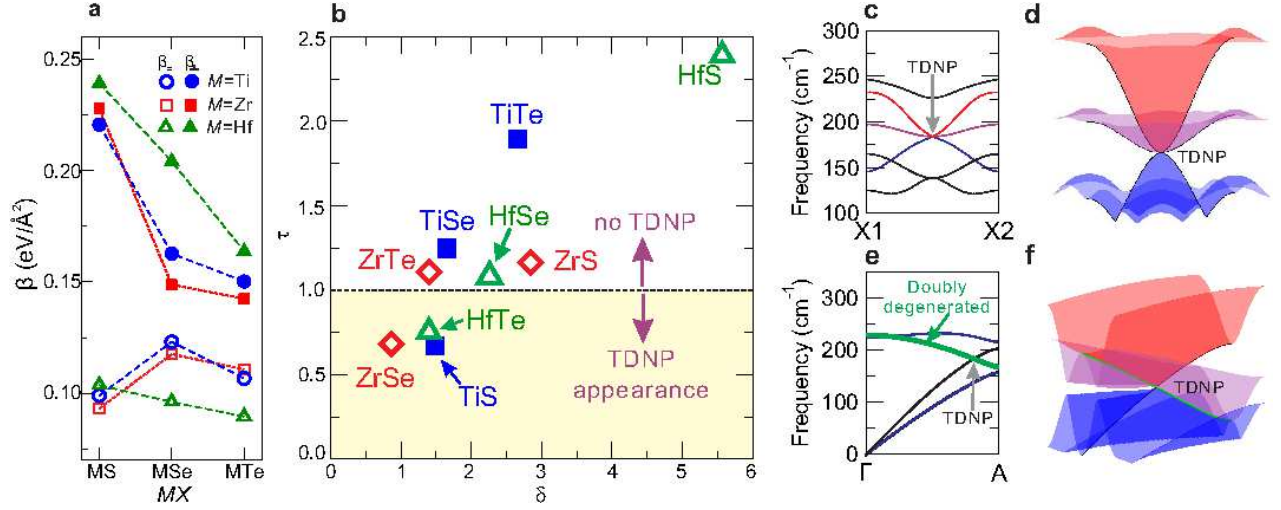


Figure 3. Second-order force constant at the A point and the dimensionless ratio τ of MX . Panel (a): DFT-derived second-order force constant at the A point for both the two-fold degenerate planar vibrational Mode $_{\pm y}^x$ and the vibrational Mode $_{\pm z}^z$. Panel (b): The derived parameter τ from Equ. (1) as a function of the δ value, as defined in the main text, for all nine compounds. Panels (c and e): DFT-derived phonon dispersions to elucidate phonon TDNPs of ZrSe along the X1 ($-\pi/2, 0, 0$) to X2 ($\pi/2, 0, 0$) and Γ -A directions, respectively. Panels (d and f): Zoom-in 3D visualization of phonon TDNPs in the $k_z = 0$ and $k_y = 0$ planes, respectively.

the integration of Berry curvature using a closed surface surrounding a node within the framework of the Wilson-loop method [108, 109]. For instance, Fig. 4(d and e) shows the Wannier center evolutions around WP3+ and WP2- with the topological positive and negative charges, respectively. Their corresponding Berry curvatures are shown in Fig. 4(f and g), indicating that the positive and negative charges, WP3+ and WP2-, have different winding directions of their Berry curvatures. Furthermore, we determine the charges of all the WPs of TiS in Table I. In similarity, ZrSe shares the same six pairs of WPs (5 pairs for type-I ones and a pair for type-II one) in Fig. 4b whereas HfTe only has four pairs of type-I WPs in Fig. 4c, whose coordinators are given in Table I. This difference is mainly because in HfTe the phonon dispersions from K to H are lacking of two band crossings, C3 at K and C6 at H.

Certainly, the existence of these WPs gives rise to the topologically protected non-trivial surface states (TPSSs) of the surface phonon dispersions. As shown in Fig. 5(a, b and c), we have calculated the surface phonon spectrum of the $(10\bar{1}0)$ surface of TiS along the high-symmetry momentum paths in the surface BZ. In particular, in order to see the projections of all WPs on the $(10\bar{1}0)$ surface, we have plot the surface phonon dispersions (Fig. 5(b and c)) along the \bar{K} - \bar{H} direction, as defined in the $(10\bar{1}0)$ surface BZ (Fig. 5d). This \bar{K} - \bar{H} direction indeed is the projection of the K-H direction in the bulk BZ. As evidenced in Fig. 5b, the three type-I WPs, WP1, WP2, and WP3, are clearly demonstrated and the other two type-I WP4 and WP5 as well as another type-II WP6 can be apparently seen in the Fig. 5c. Accordingly, we have observed the interesting TPSSs, which are typically connecting each

WP in 5(b and c). We further plot their 2D visualization of their phonon density of states (PDOSs) in Fig. 5(d to i) using the exact frequencies with 361.22 cm^{-1} of WP1, 349.10 cm^{-1} of WP2, 289.21 cm^{-1} of WP3, 242.05 cm^{-1} of WP4, 238.37 cm^{-1} of WP5, and 231.30 cm^{-1} of WP6, respectively. Interestingly, at each frequency for the $(10\bar{1}0)$ surface in Fig. 5(d to i), the TPSSs featured by the broken surface arcs connecting two WPs with opposite charges for WP1, WP2, WP3 and WP6 can be clearly visualized. However, it is a bit difficult to observe the broken arcs states connecting WP4 and WP5 on the $(10\bar{1}0)$ surface because they are heavily overlapped with the projections of bulk phonon states. The case of ZrSe also exhibits the quite similar arc states of surface phonon on its $(10\bar{1}0)$ surface (not shown here).

As compared with both cases of both TiS and ZrSe, HfTe exhibits some differences. HfTe only has four pairs of type-I WPs as marked in Fig. 4c and no type-II WPs. Fig. 6 shows its phonon spectrum of the $(10\bar{1}0)$ surface and the 2D visualizations of the PDOSs with the frequencies of 172.95 cm^{-1} of WP1, 169.95 cm^{-1} of WP2, 101.67 cm^{-1} of WP4, and 94.99 cm^{-1} of WP5, respectively. The bulk WPs are also projected onto the $(10\bar{1}0)$ surface. As shown Fig. 6b, the broken arc states of the TPSSs are clearly linked to the pair of WP1 with opposite topological charges, and only partial for both WP2 and WP4 in Fig. 6(c and d), and not observable for WP5 due to its overlapping with the projected states of bulk phonon dispersions in Fig. 6e. In addition, it still needs to be emphasized that the arc states can be certainly observed on some other planes which are paralleling to the bulk H-K direction, such as the $(01\bar{1}0)$ plane. However, note that the arc states connecting Weyl nodes cannot

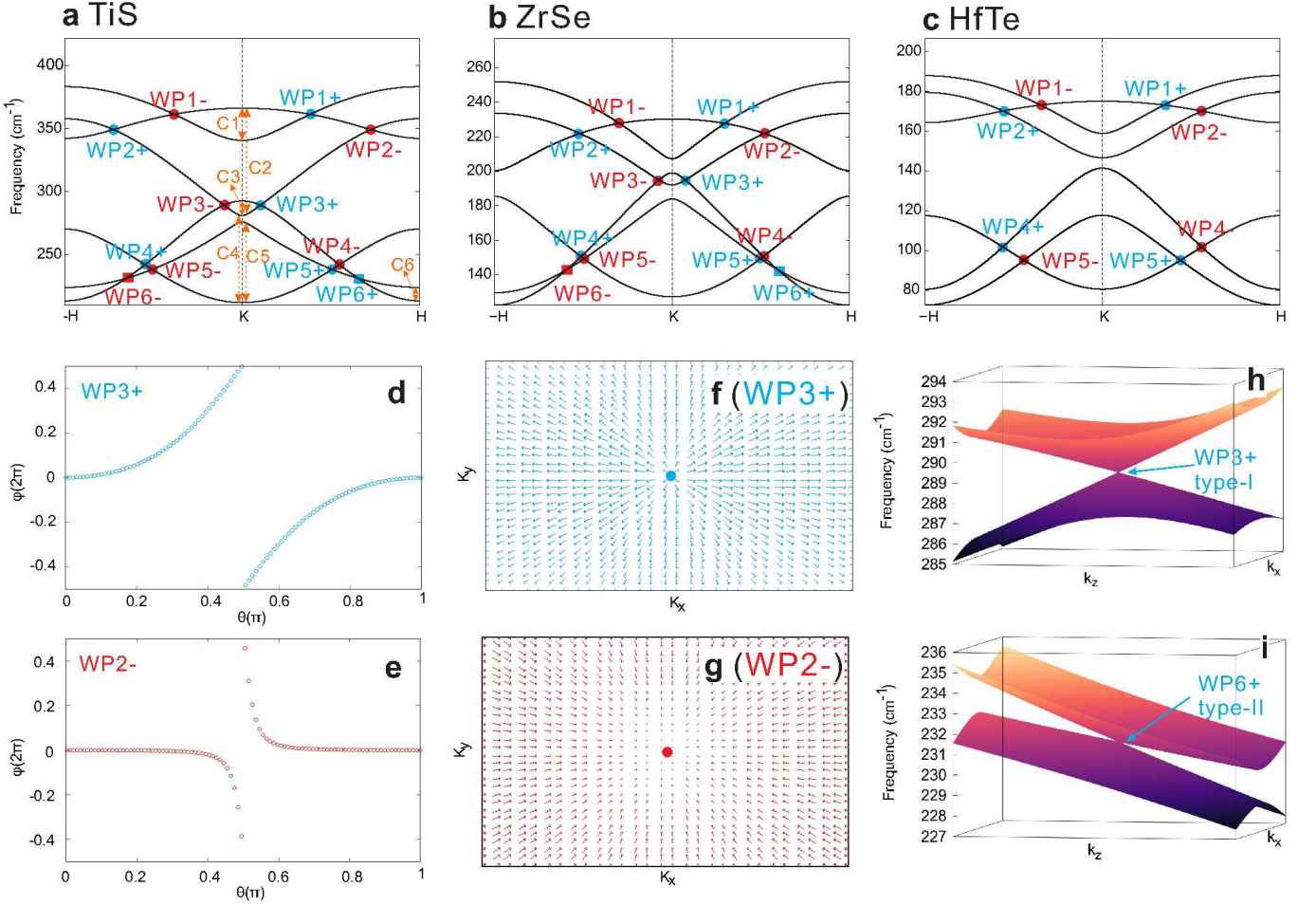


Figure 4. Topological phonons of TiS, ZrSe and HfTe. Panels (a, b and c): DFT-derived phonon dispersions along K to H for TiS, ZrSe and HfTe, respectively. Panels (d and e) show the Wannier center evolutions around positive charge WP3+ and negative charge WP2- nodes for TiS, respectively. Panels (f and g) denote the Berry curvature distributions around WP3+ and WP2- Weyl nodes for TiS. Panels (h and i) show the phonon dispersions around a type-I WP3+ and a type-II WP6+ Weyl node for TiS, respectively. Note that the symbols of WP1~WP6 are the Weyl nodes, the symbols of C1 to C6 refer to six different band crossings, and the signs of + and - denote the topological positive and negative charges, respectively.

be observable on the (0001) surface because, on it, the projections of the K-H direction coincide at the same surface momentum, and their topological charges cancel to each other.

IV. DISCUSSIONS

Through the DFT-derived results, these three materials of TiS, ZrSe and HfTe are highly attractive because of the occurrence of the coexisted TDNPs and WPs. In the first, the TDNPs of their phonons are interesting because (i) they provide a good platform to study the behaviors of the basic triple degenerate boson, one of elementary particles, in the real materials, (ii) they are highly robust, which are locked by the threefold rotational symmetry of the hexagonal lattices, and (iii) they exactly occur in the optical-acoustic gap and do not overlap with other phonon bands. Perhaps, the thermal-excited signals re-

lated with these TDNPs will not be interfered by other vibrational modes, thereby highlight the viable cases to experimentally probe the TDNP-related properties.

In the second, it is well-known that in the electronic structures the WPs and their associated topological invariants enable the corresponding materials to exhibit a variety of novel properties, such as robust surface states and chiral anomaly [17–35]. In our current cases, the existence of the bulk phononic WPs and their robust TPSSs render them to be very charming for possible applications, because these states can not be backscattered. In particular, as evidenced in Fig. 5j the surface broken arc states connecting a pair of WP1 nodes in TiS exhibit an nearly one-way propagation. Its evolution further extends and shift to the zone boundary with increasing the frequencies in a relatively wide region of frequency in Fig. 5j. In similarity, the nearly one-way arc states connecting a pair of WP1 nodes in HfTe can be clearly visualized in Fig. 6f. However, the evolution of the surface arc states

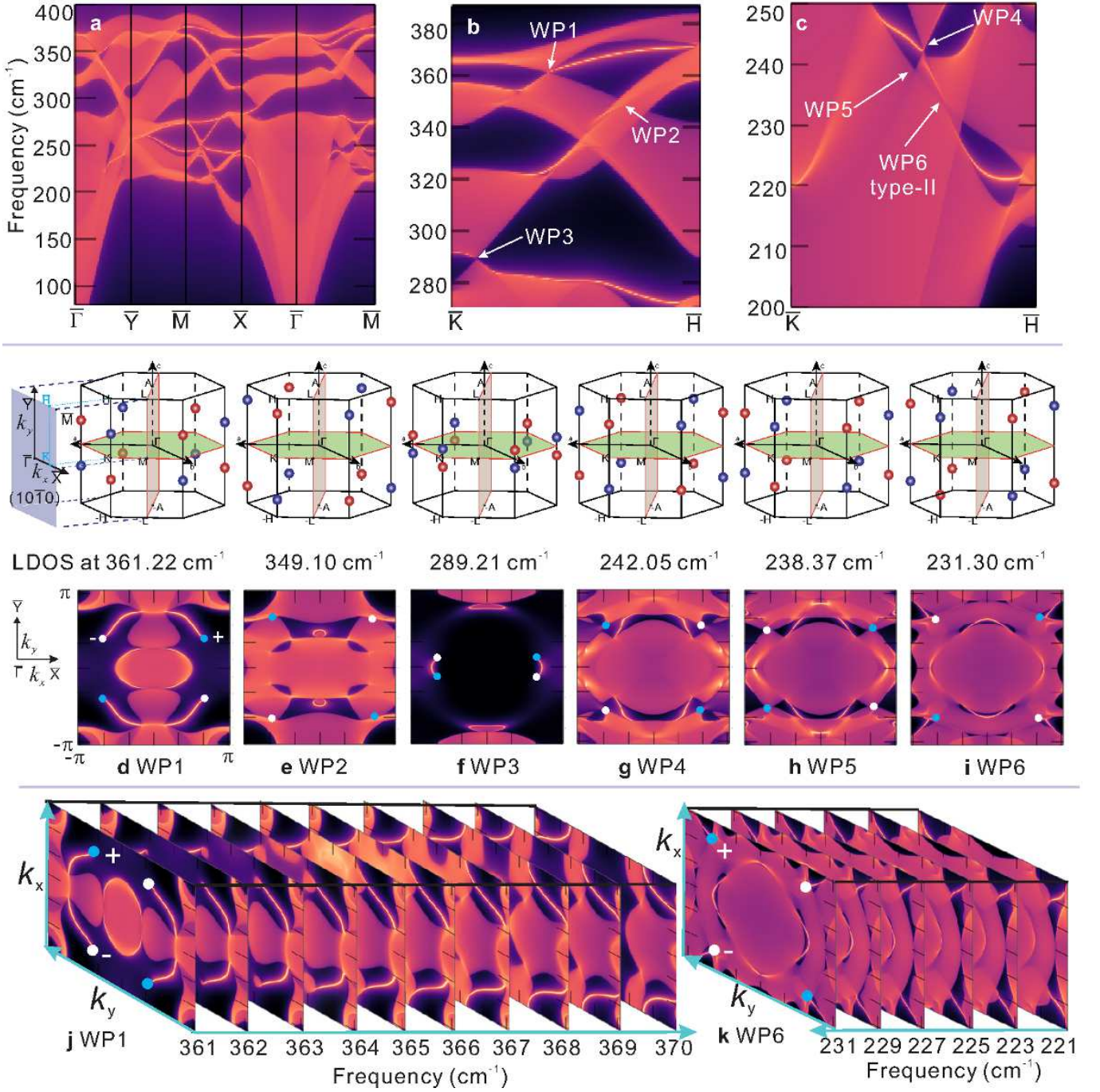


Figure 5. The surface phonon spectra and the surface phonon densities of states (PDOSs) of the $(10\bar{1}0)$ surface of TiS. Panels (a, b, c): the surface phonon spectra along the high-symmetry lines in panel (a) and along the defined $\bar{K}-\bar{H}$ line of the BZ in the $(10\bar{1}0)$ surface. Panel (d to e): the surface PDOSs at the six frequencies that the six pairs of Weyl nodes have and the projections of these bulk WPs are marked as solid blue (positive topological charge) and white (negative topological charge) circles in each panel. The surface opening arc states connect two WPs with opposite charges can be visualized in panels (d to i). Panels j and k: the frequency-dependent evolutions of the arc states connecting the type-I WP1 and the type-II WP6 on the $(10\bar{1}0)$ surface of TiS, respectively.

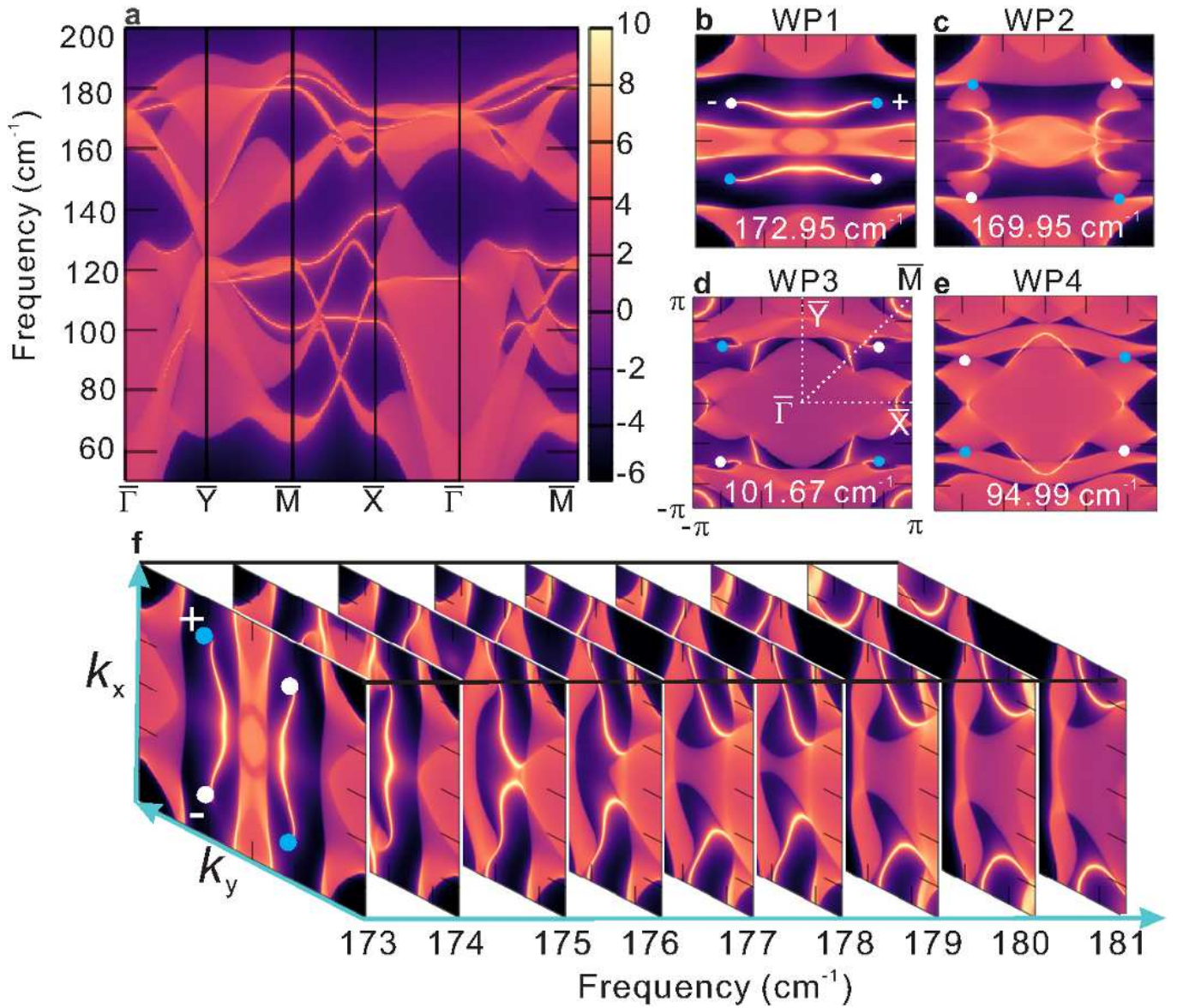


Figure 6. The surface phonon dispersion and its evolution of the PDOSs on the the $(10\bar{1}0)$ surface of HfTe. Panel (a): The surface phonon dispersion on the $(10\bar{1}0)$ surface of HfTe. Panels (b to e): The surface phonon densities of states (PDOS) at the frequencies of four pairs of Weyl nodes (WP1, WP2, WP4 and WP5 in HfTe). The projections (solid white circles - negative charge and solid blue circles - positive charge) of the bulk WPs (and their symmetric counterparts) on the $(10\bar{1}0)$ surface are indicated on each figure. The surface arcs connect two WPs with opposite charges. Panel f: the frequency-dependent evolutions of the arc states connecting the type-I WP1 on the $(10\bar{1}0)$ surface of HfTe.

Table I. Weyl points at $\mathbf{k} = (\frac{1}{3}, \frac{1}{3}, k_z)$ and their frequencies ω , topological charges (+ or -) and types (type-I or type-II) of TiS, ZrSe and HfTe.

WPs	k_z	ω (cm ⁻¹)	Charge	Type	k_z	ω (cm ⁻¹)	Charge	Type	k_z	ω (cm ⁻¹)	Charge	Type
WP1	0.1919	361.22	+	I	0.1485	227.76	+	I	0.1739	172.95	+	I
WP2	0.3628	349.07	-	I	0.2600	221.91	-	I	0.2798	169.95	-	I
WP3	0.0517	289.21	+	I	0.0371	194.93	+	I				
WP4	0.2741	242.05	-	I	0.2569	150.52	-	I	0.2803	101.67	-	I
WP5	0.2533	238.37	+	I	0.2486	149.22	+	I	0.2205	94.99	+	I
WP6	0.3265	231.30	+	II	0.2977	142.84	+	II				

connecting a pair of type-II WP6 in TiS cannot be fully visualized because most of them are overlapped with the

projections of the bulk phonon states in Fig. 5k.

V. SUMMARY

Summarizing, through first-principles calculations we have revealed that three WC-type materials of TiS, ZrSe and HfTe not only host three-component bosons featured by TDNPs and two-component Weyl bosons featured by WPs in their phonon spectra. In both TiS and ZrSe, there exist six pairs of bulk WPs (five type-I nodes and one type-II node) locating at the K-H line in the BZ, whereas in HfTe only four pairs of type-I WPs exist. We have demonstrated that their phonon spectra of these three cases are topological in nature, exhibiting that the topologically protected non-trivial surface arc states of phonons. These non-trivial states are directly linked

with various WPs with opposite chirality. Interestingly, these three cases still exhibit three-component fermions featured by TDNPs and six pairs of two-component Weyl fermions (WPs) in their electronic structures of the bulk crystals. The novel coexistence of the main features of (i) three-component bosons, (ii) two-component Weyl bosons, and three-component fermions, and (iii) two-component Weyl fermions and, in particular, both three-component bosons and three-component fermions at the nearly same momentum (Fig. 1(c and d)) along the Γ -A direction could couple to each other through electron-phonon interactions. They hence highlight a wonderful platform to study the interplays between different types of topological electron excitations and topological phonons within the atomistic scale for potential multifunctionality quantum-mechanical properties.

-
- [1] Weng, H.M., Dai, X., & Fang, Z. Topological semimetals predicted from first-principles calculations, *J. Phys. Condens. Matter.* **28**,303001 (2016).
 - [2] Yan, B.H. & Felser, C. Topological Materials: Weyl semimetals, *Annu. Rev. Condens. Matter Phys.* **8**, 337–354 (2016).
 - [3] Chiu, C.-K., Teo, J. C. Y., Schnyder, A. P. & Ryu, S. Classification of topological quantum matter with symmetries, *Rev. Mod. Phys.* **88**, 035005 (2016).
 - [4] Bansil, A., Lin, H., & Das, T. Colloquium: Topological band theory, *Rev. Mod. Phys.* **88**, 021004 (2016).
 - [5] Rao, S. Weyl semi-metals: A short review, arXiv:1603.02821 (2016).
 - [6] Wang, Z. J., Sun, Y., Chen, X.-Q., Franchini, C., Xu, G., Weng, H. M., Dai, X. & Fang, Z. Dirac semimetal and topological phase transitions in A_3Bi ($A = Na, K, Rb$), *Phys. Rev. B* **85**, 195320 (2012).
 - [7] Young, S. M., Zaheer, S., Teo, J. C. Y., Kane, C. L., Mele, E. J. & Rappe, A. M. Dirac Semimetal in Three Dimension. *Phys. Rev. Lett.* **108**, 140405 (2012).
 - [8] Wang, Z., Weng, H., Wu, Q., Dai, X. & Fang, Z. Three dimensional Dirac semimetal and quantum transport in Cd_3As_2 , *Phys. Rev. B* **88**, 125427 (2013).
 - [9] Cheng, X. Y., Li, R. H., Sun, Y., Chen, X.-Q., Li, D. Z. & Li, Y. Y. Ground-state phase in the three-dimensional topological Dirac semimetal Na_3Bi . *Phys. Rev. B* **89**, 245201 (2014).
 - [10] Neupane, M., Xu, S. Y., Sankar, R., Alidoust, N., Bian, G., Liu, C., Belopolski, I., Chang, T. R., Jeng, H. T., Lin, H., Bansil, A., Chou, F. & Hasan, M. Z. Observation of a three-dimensional topological Dirac semimetal phase in high-mobility Cd_3As_2 . *Nat. Commun.* **5**, 3786 (2014).
 - [11] Liu, Z. K., Jiang, J., Zhou, B., Wang, Z.J., Zhang, Y., Weng, H. M., Prabhakaran, D., Mo, S.-K., Peng, H., Dudin, P., Kim, T., Hoesch, M., Fang, Z., Dai, X., Shen, Z. X., Feng, D. L., Hussain, Z., & Chen, Y. L. A stable three-dimensional topological Dirac semimetal Cd_3As_2 . *Nature Mater.* **13**, 677 (2014).
 - [12] Liu, Z. K., Zhou, B., Zhang, Y., Wang, Z. J., Weng, H. M., Prabhakaran, D., Mo, S.-K., Shen, Z. X., Fang, Z., Dai, X., Hussain, Z. & Chen, Y. L. Discovery of a Three-Dimensional Topological Dirac Semimetal, Na_3Bi . *Science* **343**, 864-867 (2014).
 - [13] Yang, B. J. & Nagaosa, N. Classification of stable three dimensional Dirac semimetals with nontrivial topology, *Nat. Commun.* **5**, 4898 (2014).
 - [14] Xu, S.-Y., Liu, C., Kushwaha, S. K., Sankar, R., Krizan, J. W., Belopolski, I., Neupane, M., Bian, G., Alidoust, N., Chang, T. R., Jeng, H. T., Huang, C. Y., Tsai, W. F., Lin, H., Shibaev, P. P., Chou, F. C., Cava, R. J. & Hasan, M. Z. Observation of Fermi arc surface states in a topological metal. *Science* **347**, 294-298 (2015).
 - [15] Du, Y., Wan, B., Wang, D., Sheng, L., Duan, C.G., & Wan, X.G. Dirac and Weyl Semimetal in $XYBi$ ($X = Ba, Eu$; $Y = Cu, Ag$ and Au). *Sci. Rep.* **5**, 14423 (2015).
 - [16] Hu, J., Zhu, Y.L., Graf, D., Tang, Z.J., Liu, J.Y., & Mao, Z.Q. Quantum oscillation studies of topological semimetal candidate $ZrGeM$ ($M = S, Se, Te$), *Phys. Rev. B* **95**, 205134 (2017).
 - [17] Murakami, S. Phase transition between the quantum spin Hall and insulator phases in 3d: Emergence of a topological gapless phase, *New J. Phys.* **9**, 356 (2007).
 - [18] Wan, X.G., Turner, A. M., Vishwanath, A. & Savrasov, S. Y. Topological semimetal and Fermi-arc surface states in the electronic structure of pyrochlore iridates, *Phys. Rev. B* **83**, 205101 (2011).
 - [19] Xu, G., Weng, H., Wang, Z., Dai, X. & Fang, Z. Chern Semimetal and the Quantized Anomalous Hall Effect in $HgCr_2Se_4$, *Phys. Rev. Lett.* **107**, 186806 (2011).
 - [20] Xu, S.-Y., Alidoust, N., Belopolski, I., Yuan, Z., Bian, G., Chang, T.-R., Zheng, H., Strocov, V. N., Sanchez, D. S., Chang, G., Zhang, C., Mou, D., Wu, Y., Huang, L., Lee, C.-C., Huang, S.-M., Wang, B., Bansil, A., Jeng, H.-T., Neupert, T., Kaminski, A., Lin, H., Jia, S. & Hasan, M. Z. Discovery of a Weyl fermion state with Fermi arcs in niobium arsenide. *Nature Phys.* **11**, 748-754 (2015).
 - [21] Shekhar, C., Nayak, A. K., Sun, Y., Schmidt, M., Nicklas, M., Leermakers, I., Zeitler, U., Skourski, Y., Wosnitza, J., Liu, Z.K., Chen, Y.L., Schnelle, W., Borrmann, H., Grin, Y., & Felser, C. & Yan, B.H. Ex-

- tremely large magnetoresistance and ultrahigh mobility in the topological Weyl semimetal candidate NbP. *Nature Phys.* **11**, 645-649 (2015)
- [22] Xu, S.-Y., Belopolski, I., Sanchez, D. S., Guo, C., Chang, G., Zhang, C., Bian, G., Yuan, Z., Lu, H., Feng, Y., Chang, T.-R., Shibaev, P. P., Prokopovych, M. L., Alidoust N., Zheng, H., Lee, C.-C., Huang, S.-M., Sankar, R., Chou, F., Hsu, C.-H., Jeng, H.-T., Bansil, A., Neupert, T., Strocov, V. N., Lin, H., Jia, S. & Hasan, M. Z. Experimental discovery of a topological Weyl semimetal state in TaP. *Sci. Adv.* **1**, e1501092 (2015).
- [23] Weng, H.M., Fang, C., Fang, Z., Bernevig, B. A. & Dai, X. Weyl Semimetal Phase in Noncentrosymmetric Transition-Metal Monophosphides, *Phys. Rev. X* **5**, 011029 (2015).
- [24] Huang, S.M., Xu, S.Y., Belopolski, I., Lee, C.C., Chang, G., Wang, B.K., Alidoust, N., Bian, G., Neupane, M., Zhang, C., Jia, S., Bansil, A., Lin, H. & Hasan, M.Z. A Weyl Fermion semimetal with surface Fermi arcs in the transition metal monpnictide TaAs class, *Nat. Commun.* **6**, 7373 (2015).
- [25] Lv, B.Q., Weng, H. M., Fu, B.B., Wang, X. P., Miao, H., Ma, J., Richard, P., Huang, X. C., Zhao, L. X., Chen, G. F., Fang, Z., Dai, X., Qian, T. & Ding, H. Experimental Discovery of Weyl Semimetal TaAs, *Phys. Rev. X* **5**, 031013 (2015).
- [26] Lv, B.Q., Xu, N., Weng, H. M., Ma, J. Z., Richard, P., Huang, X.C., Zhao, L.X., Chen, G.F., Matt, C.E., Bisti, F., Strocov V.N., Mesot, J., Fang, Z., Dai, X., Qian, T., Shi, M. & Ding, H. Observation of Weyl nodes in TaAs, *Nature Phys.* **11**, 724-728 (2015).
- [27] Xu, S.-Y., Belopolski, I., Alidoust, N., Neupane, M., Bian, G., Zhang, C., Sankar, R., Chang, G., Yuan, Z., Lee, C.-C., Huang, S.-M., Zheng, H., Ma, J., Sanchez, D. S., Wang, B., Bansil, A., Chou, F., Shibaev, P.P., Lin, H., Jia, S. & Hasan, M. Z. Discovery of a Weyl fermion semimetal and topological Fermi arcs, *Science* **349**, 613-617 (2015).
- [28] Yang, L., Liu, Z., Sun, Y., Peng, H., Yang, H., Zhang, T., Zhou, B., Zhang, Y., Guo, Y., Rahn, M., Prabhakaran, D., Hussain, Z., Mo, S.-K., Felser, C., Yan, B.H. & Chen, Y.L. Weyl semimetal phase in the non-centrosymmetric compound TaAs, *Nature Phys.* **11**, 728-734 (2015).
- [29] Zhang, Y., Bulmash, D., Hosur, P., Potter, A. C. & Vishwanath, A. Quantum oscillations from generic surface Fermi arcs and bulk chiral modes in Weyl semimetals, *Sci. Rep.* **6**, 23741 (2016).
- [30] Soluyanov, A. A., Gresch, D., Wang, Z.J., Wu, Q., Troyer, M., Dai, X. & Bernevig, B. A. Type-II Weyl semimetals, *Nature* **527**, 495-498 (2015).
- [31] Xu, S.Y., Alidoust, N., Chang, G., Lu, H., Singh, B., Belopolski, I., Sanchez, D., Zhang, X., Bian, G., Zheng, H., & Hsuanu, M.A. Discovery of Lorentz-violating Weyl fermion semimetal state in LaAlGe materials. arXiv preprint arXiv:1603.07318, (2016).
- [32] Chang, G., Singh, B., Xu, S.Y., Bian, G., Huang, S.M., Hsu, C.H., Belopolski, I., Alidoust, N., Sanchez, D.S., Zheng, H., & Lu, H. Magnetic and noncentrosymmetric Weyl fermion semimetals in the RAlX family of compounds (R= rare earth, Al= aluminium, X= Si, Ge). arXiv preprint arXiv:1604.02124, (2016).
- [33] Yang, H., Sun, Y., Zhang, Y., Shi, W.J., Parkin, S.S., & Yan, B.H. Topological Weyl semimetals in the chiral antiferromagnetic materials Mn₃Ge and Mn₃Sn. *New J. Phys.* **19**, 015008 (2017).
- [34] Singh, B., Sharma, A., Lin, H., Hasan, M.Z., Prasad, R., & Bansil, A. Topological electronic structure and Weyl semimetal in the TlBiSe₂ class of semiconductors. *Phys. Rev. B* **86**, 115208 (2012).
- [35] Ruan, J., Jian, S.K., Yao, H., Zhang, H., Zhang, S.C. & Xing, D. Symmetry-protected ideal Weyl semimetal in HgTe-class materials. *Nat. Commun.* **7**, 11136 (2016).
- [36] Son, D.T., & Spivak, B. Z. Chiral anomaly and classical negative magnetoresistance of Weyl metals, *Phys. Rev. B* **88**, 104412 (2013).
- [37] Huang, X., Zhao, L., Long, Y., Wang, P., Chen, D., Yang, Z., Liang, H., Xue, M., Weng, H., Fang, Z., Dai, X. & Chen, G. Observation of the Chiral-Anomaly-Induced Negative Magnetoresistance in 3D Weyl Semimetal TaAs, *Phys. Rev. X* **5**, 031023 (2015).
- [38] Hosur, P. & Qi, X. Recent developments in transport phenomena in Weyl semimetals, *C. R. Phys.* **14**, 857-870 (2013).
- [39] Fang, C., Weng, H. M., Dai, X. & Fang, Z. Topological nodal line semimetals. *Chin. Phys. B* **25**, 117106 (2016).
- [40] Ryu, S. & Hatsugai, Y. Topological Origin of Zero-Energy Edge States in Particle-Hole Symmetric Systems. *Phys. Rev. Lett.* **89**, 077002 (2002).
- [41] Heikkilä, T. T. & Volovik, G. E. Dimensional crossover in topological matter: Evolution of the multiple Dirac point in the layered system to the flat band on the surface. *JETP Lett.* **93**, 59-65 (2011).
- [42] Burkov, A. A., Hook, M. D. & Balents, L. Topological nodal semimetals. *Phys. Rev. B* **84**, 235126 (2011).
- [43] Li, R. H., Ma, H., Cheng, X. Y., Wang, S. L., Li, D. Z., Zhang, Z. Y., Li, Y. Y. & Chen, X.-Q. Dirac node lines in pure alkali earth metals. *Phys. Rev. Lett.* **117**, 096401 (2016).
- [44] Weng, H. M., Liang, Y. Y., Xu, Q. N., Yu, R., Fang, Z., Dai, X. & Kawazoe, Y. Topological node-line semimetal in three dimensional graphene networks. *Phys. Rev. B* **92**, 045108 (2015).
- [45] Yu, R., Weng, H. M., Fang, Z., Dai, X. & Hu, X. Topological Node-Line Semimetal and Dirac Semimetal State in Antiperovskite Cu₃PdN. *Phys. Rev. Lett.* **115**, 036807 (2015).
- [46] Kim, Y., Wieder, B. J., Kane, C. L. & Rappe, A. M. Dirac Line Nodes in Inversion-Symmetric Crystals. *Phys. Rev. Lett.* **115**, 036806 (2015).
- [47] Xie, L. S., Schoop, L. M., Seibel, E. M., Gibson, Q. D., Xie, W. W. & Cava, R. J. A new form of Ca₃P₂ with a ring of Dirac nodes. *APL Materials* **3**, 083602 (2015).
- [48] Zeng, M. G., Fang, C., Chang, G. Q., Chen, Y.-A., Hsieh, T., Bansil, A., Lin, H. & Fu, L. Topological semimetals and topological insulators in rare earth monpnictides. Preprint at <https://arxiv.org/abs/1504.03492> (2015).
- [49] Mullen, K., Uchoa, B. & Glatzhofer, D. T. Line of Dirac Nodes in Hyperhoneycomb Lattices. *Phys. Rev. Lett.* **115**, 026403 (2015).
- [50] Gan, L.-Y., Wang, R., Jin, Y. J., Ling, D. B., Zhao, J. Z., Xu, W.P., Liu, J. F. & Xu, H. Pressure-induced Topological Node-Line Semimetals in Alkaline-Earth Hexaborides XB₆ (X=Ca, Sr, Ba). Preprint at <https://arxiv.org/abs/1611.06386> (2016).
- [51] Kawakami, T. & Hu, X. Symmetry-Guaranteed and

- Accidental Nodal-Line Semimetals in FCC Lattice. Preprint at <https://arxiv.org/abs/1611.07342> (2016).
- [52] Yang, B., Zhou, H. C., Zhang, X. M., Liu, X. B. & Zhao, M. W. Dirac cones and highly anisotropic electronic structure of supergraphyne. *Carbon* **113**, 40-45 (2017).
- [53] Li, J.X., Ma, H., Feng, S., Ullah, S., Li, R., Dong, J. & Chen, X.-Q. Topological nodal line states and a potential catalyst of hydrogen evolution in the TiSi family. arXiv preprint arXiv:1704.07043 (2017).
- [54] Bradlyn, B., Cano, J., Wang, Z., Vergniory, M. G., Felser, C., Cava, R. J. & Bernevig, B. A. Beyond Dirac and Weyl fermions: Unconventional quasiparticles in conventional crystals, *Science* **353**, 558 (2016).
- [55] Winkler, G. W., Wu, Q., Troyer, M., Krogstrup, P. & Soluyanov, A. A. Topological Phases in $\text{InAs}_{1-x}\text{Sb}_x$: From Novel Topological Semimetal to Majorana Wire, *Phys. Rev. Lett.* **117**, 076403 (2016).
- [56] Weng, H., Fang, C., Fang, Z. & Dai, X. Topological semimetals with triply degenerate nodal points in θ -phase tantalum nitride, *Phys. Rev. B* **93**, 241202 (2016).
- [57] Weng, H., Fang, C., Fang, Z. & Dai, X. Coexistence of Weyl fermion and massless triply degenerate nodal points, *Phys. Rev. B* **94**, 165201 (2016).
- [58] Zhu, Z., Winkler, G. W., Wu, Q. S., Li, J. & Soluyanov, A. A. Triple point topological metals. *Phys. Rev. X* **6**, 031003 (2016).
- [59] Chang, G., Xu, S.Y., Huang, S.M., Sanchez, D.S., Hsu, C.H., Bian, G., Yu, Z.M., Belopolski, I., Alidoust, N., Zheng, H., Chang, T.R., Jeng, H.J., Yang, S.A., Neupert, T., Lin, H. & Hasan, M.Z. New fermions on the line in topological symmorphic metals. *Sci. Rep.* **7**, 1688 (2017).
- [60] He, J. B., Chen, D., Zhu, W. L., Zhang, S., Zhao, L. X., Ren, Z. A. & Chen, G. F. Magnetotransport properties of the triply degenerate node topological semimetal: tungsten carbide. *Phys. Rev. B* **95**, 195165 (2017).
- [61] Lv, B.Q., Feng, Z.L., Xu, Q.N., Gao, X., Ma, J.Z., Kong, L.K., Richard, P., Huang, Y.B., Strocov, V. N., Fang, C., Weng, H.M., Shi, Y.G., Qian, T., & Ding, H. Observation of three-component fermions in the topological semimetal molybdenum phosphide, *Nature* **546**, 627-631 (2017).
- [62] Yang, H., Yu, J.B., Parkin, S.S.P., Felser, C., Liu, C.-X. & Yan, B.H., Prediction of triple point fermions in simple half-Heusler topological insulators, *Phys. Rev. Lett.* **119**, 136401 (2016).
- [63] Yu, J.B., Yan, B.H. & Liu, C.-X. Model Hamiltonian and time reversal breaking topological phases of antiferromagnetic half-Heusler Materials, *Phys. Rev. B* **95**, 235158 (2017).
- [64] Lu, L., Fu, L., Joannopoulos, J. D. & Soljačić, M. Weyl points and line nodes in gyroid photonic crystals. *Nature Photon.* **7**, 294-299 (2013).
- [65] Lu, L., Wang, Z., Ye, D., Ran, L., Fu, L., Joannopoulos, J. D. & Soljačić, M. Experimental observation of Weyl points, *Science* **349**, 622 (2015).
- [66] Huber, S.D. Topological mechanics. *Nature Phys.* **12**, 621-623 (2016).
- [67] Prodan, E. & Prodan, C. Topological phonon modes and their role in dynamic instability of microtubules, *Phys. Rev. Lett.* **103**, 248101 (2009).
- [68] Chen, B.G.G., Upadhyaya, N. & Vitelli, V. Nonlinear conduction via solitons in a topological mechanical insulator. *Proc Natl Acad Sci.* **111**, 13004-13009 (2014).
- [69] Yang, Z., Gao, F., Shi, X., Lin, X., Gao, Z., Chong, Y. & Zhang, B. Topological acoustics. *Phys. Rev. Lett.* **114**, 114301 (2015).
- [70] Wang, P., Lu, L. & Bertoldi, K. Topological phononic crystals with one-way elastic edge waves. *Phys. Rev. Lett.* **115**, 104302 (2015).
- [71] Xiao, M., Chen, W.J., He, W.Y. & Chan, C. T. Synthetic gauge flux and Weyl points in acoustic systems. *Nature Phys.* **11**, 920 (2015).
- [72] Nash, L. M., Kleckner, D., Read, A., Vitelli, V., Turner, A. M. & Irvine, W. T. Topological mechanics of gyroscopic metamaterials. *Proc Natl Acad Sci.* **112**, 14495-14500 (2015).
- [73] Susstrunk, R. & Huber, S. D. Observation of phononic helical edge states in a mechanical topological insulator, *Science* **349**, 47-50 (2015).
- [74] Mousavi, S. H., Khanikaev, A. B. & Wang, Z. Topologically protected elastic waves in phononic metamaterials. *Nat. Commun.* **6**, 8682 (2015).
- [75] Fleury, R., Khanikaev, A. B. & AlRu, A. Floquet topological insulators for sound, *Nat. Commun.* **7**, 11744 (2016).
- [76] Rocklin, D. Z., Chen, B.G.G., Falk, M., Vitelli, V. & Lubensky, T. Mechanical weyl modes in topological maxwell lattices. *Phys. Rev. Lett.* **116**, 135503 (2016).
- [77] He, C., Ni, X., Ge, H., Sun, X.C., Chen, Y.B., Lu, M.-H., Liu, X.P. & Chen, Y.-F. Acoustic topological insulator and robust one-way sound transport. *Nature Phys.* **12**, 1124-1129 (2016).
- [78] Susstrunk, R. & Huber, S. D. Classification of topological phonons in linear mechanical metamaterials. *Proc Natl Acad Sci.* **113**, E4767-E4775 (2016).
- [79] Li, F., Huang, X.Q., Lu, J.Y., Ma, J.H., & Liu, Z.Y., Weyl points and Fermi arcs in a chiral phononic crystal, *Nat. Phys.* DOI: 10.1038/NPYS42675 (2017).
- [80] Zhang, T.T., Song, Z.D., Alexandradinata, A., Weng, H.M., Fang, C., Lu, L. & Fang, Z. Double-Weyl phonons in transition-metal monosilicides, arXiv: 1705.07244 (2017).
- [81] Zhang, L.F. & Niu, Q., Chiral phonons at high-symmetry points in monolayer hexagonal lattices, *Phys. Rev. Lett.* **115**, 115502 (2015).
- [82] Liu, Y., Xu, Y., Zhang, S.-C., & Duan W. H., Model for topological phononics and phonon diode, *Phys. Rev. B* **96**, 064106 (2017).
- [83] Hohenberg, P. & Kohn, W. Inhomogeneous Electron Gas, *Phys. Rev.* **136**, B864-B871 (1964).
- [84] W. Kohn, and L. J. Sham, Self-Consistent Equations Including Exchange and Correlation Effects, *Phys. Rev.* **140**, A1133 (1965).
- [85] Baroni, S., Gironcoli, S.D., Corso, A.D. & Giannozzi, P. Phonons and related crystal properties from density-functional perturbation theory, *Rev. Mod. Phys.* **73**, 515 (2001).
- [86] Kresse, G. & Hafner, J. Ab initio molecular dynamics for liquid metals. *Phys. Rev. B* **47**, 558-561 (1993).
- [87] Kresse, G. & Hafner, J. Ab initio molecular-dynamics simulation of the liquid-metal amorphous-semiconductor transition in germanium. *Phys. Rev. B* **49**, 14251-14269 (1994).
- [88] Kresse, G. & Furthmüller, J. Efficiency of ab-initio total energy calculations for metals and semiconductors using a plane-wave basis set. *Comput. Mater. Sci.* **6**, 15-50

- (1996).
- [89] Perdew, J. P. & Wang, Y. Accurate and simple analytic representation of the electron-gas correlation energy, *Phys. Rev. B* **45**, 13244-13249 (1992).
 - [90] Perdew, J. P., Burke, K. & Ernzerhof, M. Generalized Gradient Approximation Made Simple, *Phys. Rev. Lett.* **77**, 3865-3868 (1996).
 - [91] Blöchl, P. E. Projector augmented-wave method, *Phys. Rev. B* **50**, 17953-17979 (1994).
 - [92] Kresse, G. & Joubert, D. From ultrasoft pseudopotentials to the projector augmented-wave method *Phys. Rev. B* **59**, 1758-1775 (1999).
 - [93] Sancho, M. P., Sancho, J. M. & Rubio, J. Highly convergent schemes for the calculation of bulk and surface Green functions, *J. Phys. F: Met. Phys.* **15**, 851-858 (1985).
 - [94] Weng, H.M., Dai, X. & Fang, Z. Exploration and prediction of topological electronic materials based on first-principles calculations, *MRS Bull.* **39**, 849-858 (2014).
 - [95] Weng, H.M., Yu, R., Hu, X., Dai, X. & Fang, Z. Quantum anomalous Hall effect and related topological electronic states, *Adv. Phys.* **64**, 227-282 (2015).
 - [96] Marzari, N. & Vanderbilt, D. Maximally localized generalized Wannier functions for composite energy bands, *Phys. Rev. B* **56**, 12847-12865 (1997).
 - [97] Souza, I., Marzari, N. & Vanderbilt, D. Maximally localized Wannier functions for entangled energy bands, *Phys. Rev. B* **65**, 035109 (2001).
 - [98] Mostofi, A. A., Yates, J. R., Lee, Y.S., Souza, I., Vanderbilt, D. & Marzari, N. Wannier90: A tool for obtaining maximally-localised Wannier functions, *Comput. Phys. Commun.* **178**, 685-699 (2008).
 - [99] Chaput, L., Togo, A., Tanaka, I. & Hug, G. Phonon-phonon interactions in transition metals, *Phys. Rev. B* **84**, 094302 (2011).
 - [100] Hahn, H. & Ness, P. Über Subchalkogenidphasen des Titans. *Z. Anorg. Allg. Chem.* **302**, 17-36 (1959).
 - [101] Hahn, H., Harder, B., Mutschke, U. & Ness, P. Zur Kristallstruktur einiger Verbindungen und Phasen des Systems Zirkon/Schwefel. *Z. Anorg. Allg. Chem.* **292**, 82-96 (1957).
 - [102] Steiger, R.P. & Cater, E.D. Preparation and identification of the ZrS phase in the zirconium-sulfur system. *High Temp. Sci.* **2**, 398-401 (1970).
 - [103] Hahn, H. & Ness, P. Über das System Zirkon/Selen. *Z. Anorg. Allg. Chem.* **302**, 37-49 (1959).
 - [104] Schewe-Miller, I. M. & Young, V. G. Hf₂Se₃, a new structure in the binary Hf-Se system. *J. Alloys Compd.* **216**, 113-115 (1994).
 - [105] Sodeck, H., Mikler, H. & Komarek, K. L. Transition metal-chalcogen systems, VI: The zirconium-tellurium phase diagram. *Monatsh Chem.* **110**, 1-8 (1979).
 - [106] Örylgsson, G. & Harbrecht, B. Structure, properties, and bonding of ZrTe (MnP type), a low-symmetry, high-temperature modification of ZrTe (WC type), *J. Am. Chem. Soc.* **123**, 4168-4173 (2001).
 - [107] Örylgsson, G. & Harbrecht, B. The crystal structure of WC type ZrTe. Advantages in chemical bonding as contrasted to NiAs type ZrTe, *Z. Naturforsch. B* **54**, 1125-1128 (1999).
 - [108] Yu, R., Qi, X. L., Bernevig, A., Fang, Z. & Dai, X. Equivalent expression of Z₂ topological invariant for band insulators using the non-Abelian Berry connection, *Phys. Rev. B* **84**, 075119 (2011).
 - [109] Soluyanov, A. A., & Vanderbilt, D., Computing topological invariants without inversion symmetry, *Phys. Rev. B* **83**, 235401 (2011).

Acknowledgments

We thank H. M. Weng for valuable discussions. Work was supported by the National Science Fund for Distinguished Young Scholars (No. 51725103), by the National Natural Science Foundation of China (Grant Nos. 51671193 and 51474202), and by the Science Challenging Project No. TZ2016004. All calculations have been performed on the high-performance computational cluster in the Shenyang National University Science and Technology Park and the National Supercomputing Center in Guangzhou (TH-2 system) with special program for applied research of the NSFC-Guangdong Joint Fund (the second phase) under Grant No.U1501501.

Supplemental Materials: "Coexisted Three-component and Two-component Weyl bosons in the topological semimetals of TiS, ZrSe and HfTe"

Jiangxu Li¹, Qing Xie^{1,2}, Sami Ullah^{1,2}, Ronghan Li¹, Hui Ma¹, Dianzhong Li¹, Yiyi Li¹, Xing-Qiu Chen^{1,*}

¹ *Shenyang National Laboratory for Materials Science, Institute of Metal Research, Chinese Academy of Science, School of Materials Science and Engineering, University of Science and Technology of China, 110016, Shenyang, China*

² *University of Chinese Academy of Sciences, Beijing, 100049, China*

* Corresponding author: xingqiu.chen@imr.ac.cn (X.-Q. C.)

Supplementary Materials

1. **Table S1:** Optimized lattice parameters of MX
2. **Figure S1:** Electronic structures of ZrSe
3. **Figure S2:** Evolution of the electronic structure around the Weyl points (WPs) in ZrSe
4. **Figure S3:** Surface electronic band structures of (0001) and (10 $\bar{1}$ 0) surfaces of ZrSe
5. **Figure S4:** Fermi surfaces of the (0001) and (10 $\bar{1}$ 0) surfaces of ZrSe
6. **Figure S5:** DFT-derived phonon dispersions of the nine MX compounds

A. Supplementary Table S1

We have optimized the lattice structures of nine MX compounds with the WC-type structure. Table S1 summarizes all optimized lattice constants as compared with the available experimental data. Among these nine compounds, five compounds of TiS, ZrS, ZrSe_{0.90}, and Hf_{0.92}Se as well as ZrTe were experimentally reported to have the same WC-type structure [100–107]. Because of no any experimental data available for the remaining four compounds of TiSe, TiTe, HfS, and HfTe, here we have assumed that they also crystallizes in the same WC-type structure. For five experimentally known compounds TiS, ZrS, ZrSe, ZrTe and HfSe, our DFT calculations yield the good agreement of their equilibrium lattice parameters with the experimental data as shown in Table S1. Furthermore, their enthalpies of formation are derived in Table S1, indicating their stabilities in the thermodynamics.

B. Electronic band structures

To elucidate the electronic band structure of these compounds, we have first repeated the calculations of ZrTe and obtained the electronic band structures are very similar to the reported data in Ref. 57, indicating the reliability of our current calculations. Remarkably, the derived electronic band structures of other compounds in this family are all similar to that of ZrTe.

We have elucidated the electronic band structures of these nine compounds. Interestingly, their electronic structures are in similarity to the case of ZrTe in Ref. 57. We have selected ZrSe as a prototypical example to show the crucial feature of electronic structures (details refer to Fig. S1-S3 in supplementary materials). Without the spin-orbit coupling (SOC) effect the two main features can be observed: In the first, a Dirac nodal line (DNL as marked in Fig. 1(c) in the main text) centered at each K point in the $K_z = 0$ plane is formed around the Fermi level due to the linear crossing of the inverted bands between the Zr $d_{xz}+d_{yz}$ orbitals and Zr $d_{x^2-y^2}+d_{xy}$ orbitals (Fig. s1(a)). In the second, a six-fold degenerate nodal point (Fig. s1(a)) locating at (0, 0, 0.3025) along the Γ -A direction around the Fermi level due to another band inversion between the doubly degenerate Zr $d_{xz}+d_{yz}$ and the Zr d_{z^2} -like orbitals at the A point of the BZ. Because the masses of both Zr and Se are not so light that their SOC effects can not be ignored. With the SOC inclusion, the derived electronic band structure clearly exhibits the apparent changes around the Fermi level: Firstly, due to the lack of inversion symmetry the spin splitting bands appears and each DNL around the K point is indeed broken into two Weyl points (WPs) with the opposite chirality (see WP+ and WP- as marked in Fig. s1(c)). In total, there are six pairs of WPs locating at both $k_z = \pm 0.01628$ plane slightly above and below the $k_z = 0$ planes. All these twelve WPs have the same energy level (Fig. s1(d)). Secondly, the SOC inclusion splits each six-fold generated nodal point into two triply degenerate nodal points (TDNP1 (0, 0, 0.2904) and TDNP2 (0, 0, 0.3146) as marked in Fig. s1(c) (their specified locations are marked in Fig. 1(c) in the main text) along the Γ to A direction. Their appearance is protected by the C_{3z} rotation and mirror symmetries, being the same as both ZrTe and TaN cases have [56, 57].

The evolution of the derived electronic band structures around one of WPs for ZrSe is illustrated in supplementary Fig. S1(a,b,c) and it can be clearly seen that the WP appears around the Fermi level in supplementary Fig. S2c. Their non-trivial topological property of the electronic bands can be identified using the Wilson loop method [108] (see Fig. S2). As shown in Fig. S2(d and e), the calculated evolution of the Wannier centers formed along the k_y direction in the two $k_z = 0$ and π planes. It can be seen that the Z_2 numbers (namely, counting the times of Wannier center crosses a reference line) of both these planes are odd, indicating their topological non-trivial feature. We have also derived the topological non-trivial (0001) and (10 $\bar{1}$ 0) Fermi-arc surface states in Figs. S3 and S4, showing the very similar non-trivial surface states to ZrTe [57]. Besides ZrSe and ZrTe, the other seven members in this family all exhibit the similar electronic structures featured with the coexisted TDNPs and WPs in their electronic structures of bulk phases.

To further clarify the topological feature in ZrSe, we have calculated the surface electronic structures on its (0001) and (10 $\bar{1}$ 0) surfaces (see supplementary Fig. S2), clearly indicating the topological surface states. In addition, we also plot the Fermi surface of both surfaces in supplementary Fig. S3. On the (0001) Fermi surface the two TDNPs along Γ to A direction in its bulk phase are both projected onto the $\bar{\Gamma}$ point, becoming invisible due to the overlapping with the projection of the bulk electronic bands. Each pair of WPs above and below the $k_z = 0$ plane which have different chirality in the bulk phase will be projected onto the same point, totally forming six projected nodes. These six projected nodes on the (0001) surface are further connected by Fermi arcs, resulting in the appearance of two triangle-like loops, as illustrated in supplementary Fig. S3(a). It is impossible to see these six projected nodes in supplementary Fig. S3(a) because their energy is 155 meV above the Fermi level. By changing the chemical potential to 155 meV, the Fermi surface gives rise to the clear visualization of six projected nodes in supplementary Fig. S3(c). In order to visualize the Weyl nodes, we further calculated (10 $\bar{1}$ 0) Fermi surface at the energy level of 155 meV above the Fermi level in supplementary Fig. S3(d). On this surface, the six pairs of WPs with opposite chirality are

Table S1. DFT-derived lattice constants a (Å) and c (Å) and enthalpy of formation (eV/atom) of single crystals, in comparison with available experimental data.

	a	c	ΔH	
TiS	3.287	3.210		Expt. Ref. 100
	3.267	3.223	-1.50	Calc.
TiSe	3.419	3.402	-1.28	Calc.
TiTe	3.669	3.656	-0.64	Calc.
ZrS	3.446	3.445		Exp. Ref. 101 and 102
	3.460	3.475	-1.65	Calc.
ZrSe _{0.90}	3.551	3.615		Exp. Ref. 103
	3.584	3.649	-1.49	Calc.
ZrTe	3.760	3.860		Exp. Ref. 105–107
	3.798	3.895	-0.91	Calc.
HfS	3.395	3.447	-1.54	Calc.
Hf _{0.92} Se	3.4958	3.6069		Exp. Ref. 104
	3.5173	3.6365	-1.32	Calc.
HfTe	3.739	3.885	-0.68	Calc.

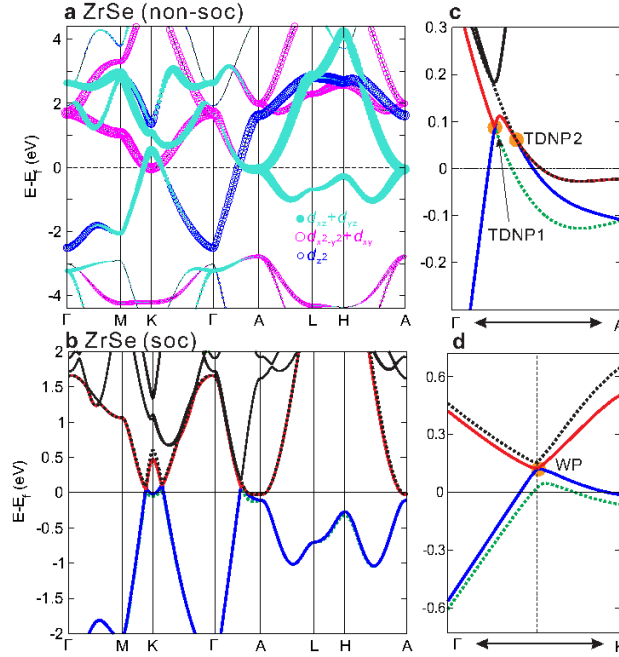


Figure S1. Electronic structures of ZrSe. Panel (a): band structure without the SOC inclusion shows (i) the band inversion between $d_{xz}+d_{yz}$ and $d_{x^2-y^2}+d_{xy}$ at K and (ii) the band inversion between d_z^2 and $d_{xz}+d_{yz}$ orbitals at A. Panel (b): Electronic band structure with the SOC inclusion. Panel (c) shows the zoom-in visualization of two TDNP1 and TDNP2 along the Γ -A direction in panel (b), whereas Panel (d) shows the zoom-in bands crossing one WP (0.27314, 0.27314, ± 0.01628) around the Fermi level with the SOC inclusion.

projected to different positions. Two WPs with same chirality are projected to the same point on the (10 $\bar{1}$ 0) surface (called WP1) and the projected points of other WPs are labeled as WP2. It can be clearly seen that the projected Weyl points are connected by Fermi arcs. For each WP1 point, there is one arc connecting it by going through the $\bar{\Gamma}$ - \bar{M} path, whereas, for each WP2 there are two arcs connecting them in supplementary Fig. S3(d). In addition, on both (0001) and (10 $\bar{1}$ 0) surfaces it is impossible to see TDNPs because the projection of TDNPs are all overlapped with bulk electronic bands, as illustrated in Fig. supplementary Fig. S3(c).

Through our calculations the other eight members in this family all exhibit the similar electronic structures with the coexisted TDNPs and WPs in their bulk phases, except for TiS. Because of the weak SOC effect, TiS is highly unique with the coexisted six Dirac nodal lines (DNLs) and two six-degenerated nodal points, which is exactly what happened for ZrSe without the SOC effect.

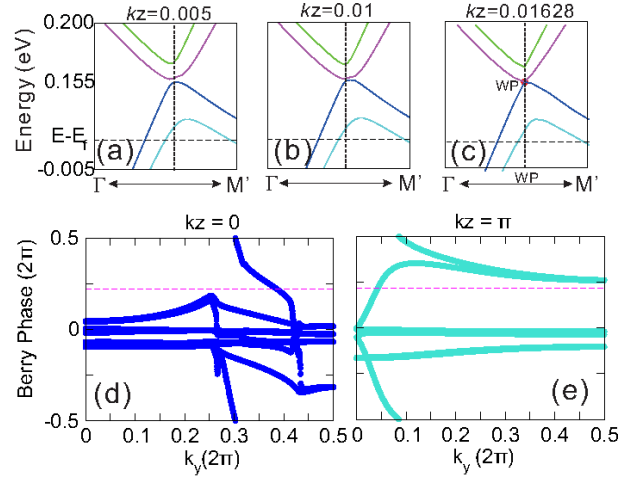


Figure S2. Electronic band structures around the WP node at $K_z = 0.005$ in panel (a), 0.010 in panel (b), and 0.01628 (exactly corresponding to the WP node) in panel (c), respectively. Panels (d and e) denote the derived Wilson loops of ZrSe which show the k_y evaluation of the Berry phases of all occupied bands along the k_x direction in both $k_z = 0$ and $k_z = \pi$ planes, respectively.

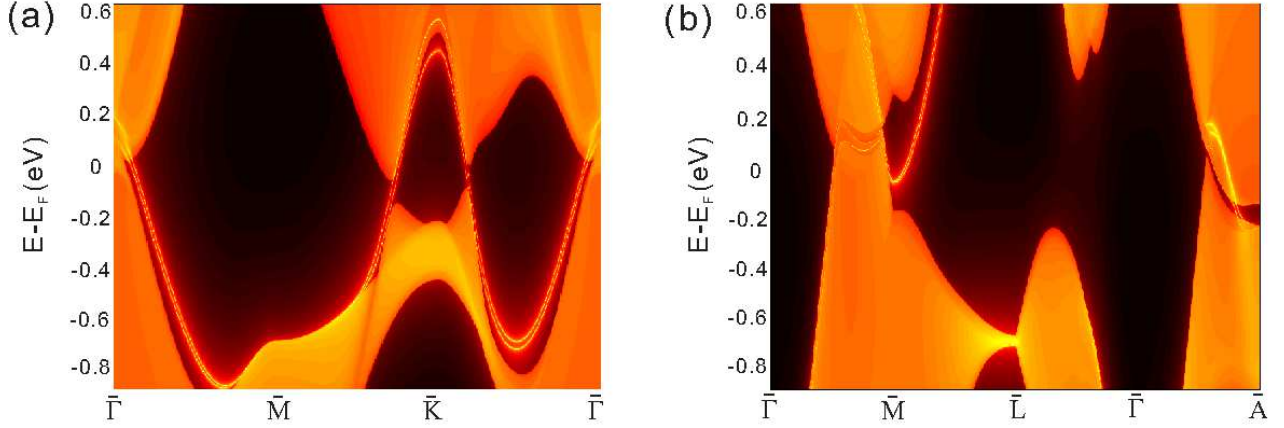


Figure S3. Calculated surface electron structures of both (0001) and (10 $\bar{1}$ 0) surfaces of ZrSe.

C. Phonon dispersions of MX

Supplementary Figure S4 compiles the DFT-derived phonon dispersions of all nine *MX* compounds. Among them, only three compounds of TiS, ZrSe and HfTe exhibit the non-trivial topological phonon states with the appearance of the triply degenerate nodal points (TDNPs as marked in supplementary Figure S4, which refers to three-component bosons).

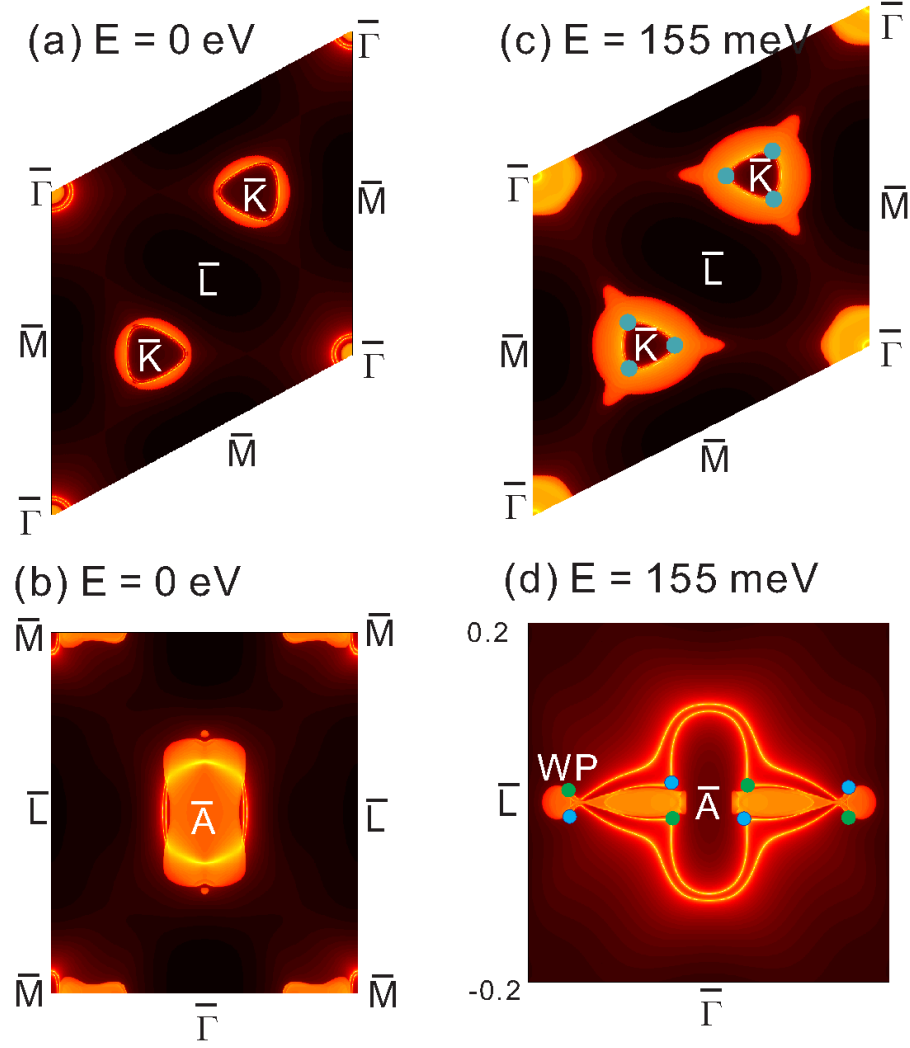


Figure S4. The Fermi surfaces of (0001) (panels: a and c) and (10 $\bar{1}$ 0) (panels: b and d) surfaces of ZrSe. Panels (a) and (b) denote the Fermi surfaces at the Fermi level, while panels (c) and (d) refer to the Fermi surfaces with a chemical potential of 155 meV above the Fermi level. The solid circles indicate the projected WPs in the (10 $\bar{1}$ 0) surfaces.

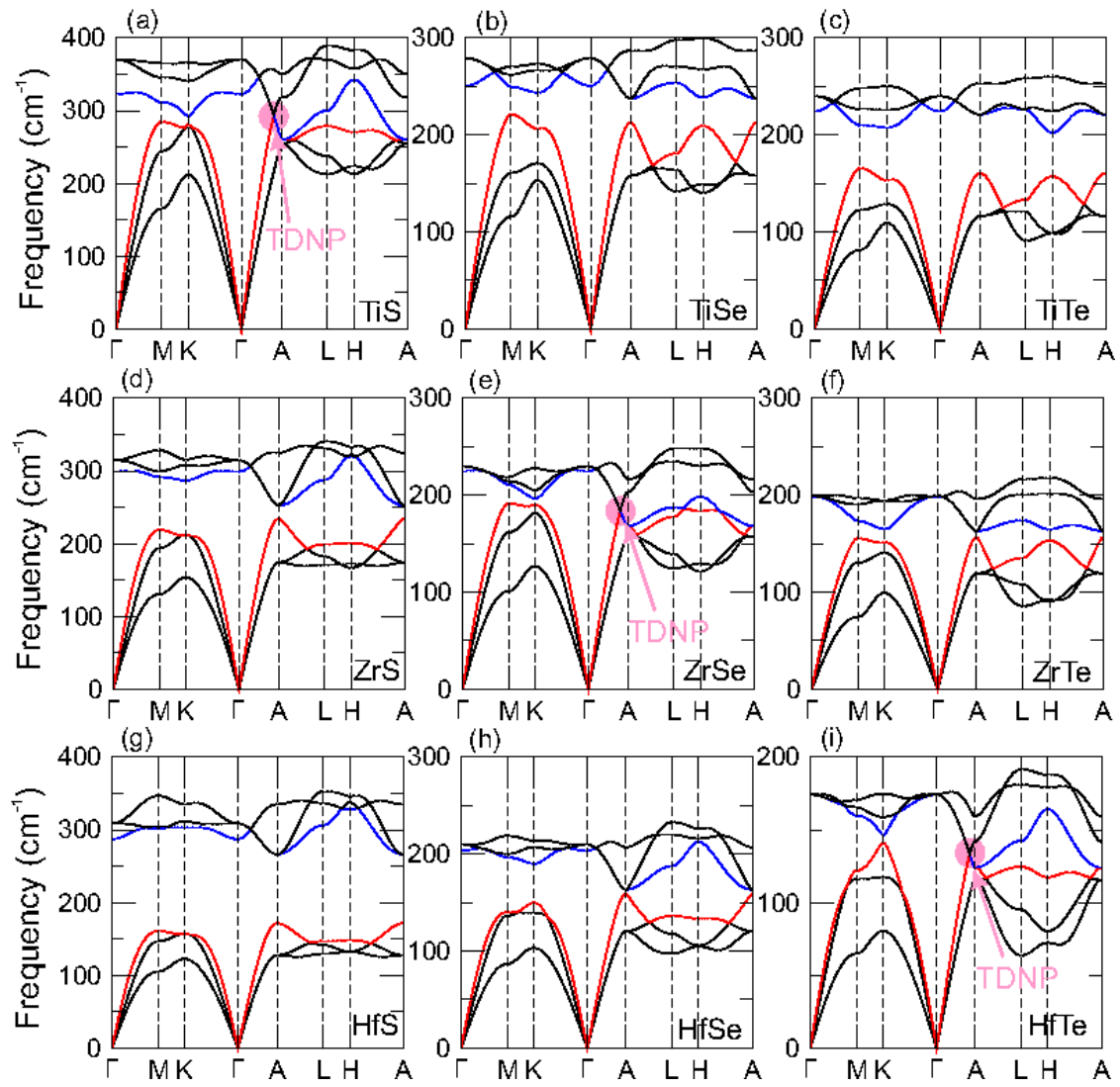


Figure S5. DFT-derived phonon dispersions of all nine *MX* compounds with the WC-type structure at their optimized equilibrium lattices.